Mapping of all polarization-singularity C-point morphologies

E.J. Galvez, B.L. Rojec, and K. Beach

Department of Physics and Astronomy, Colgate University, Hamilton, NY 13346, U.S.A.

ABSTRACT

We present theoretical descriptions and measurements of optical beams carrying isolated polarization-singularity C-points. Our analysis covers all types of C-points, including asymmetric lemons, stars and monstars. They are formed by the superposition of a circularly polarized mode carrying an optical vortex and a fundamental Gaussian mode in the opposite state of polarization. The type of C-point can be controlled experimentally by varying two parameters controlling the asymmetry of the optical vortex. This was implemented via a superposition of modes with singly charged optical vortices of opposite sign, and varying the relative amplitude and phase. The results are in excellent agreement with the predictions.

Keywords: Polarization singularities, C-points, Poincaré beams

1. INTRODUCTION

Recent research in complex light has brought increased interest in polarization singularities.[1–3] They appear as non-separable superpositions of polarization and spatial modes in prepared beams,[4,5] or as the result of inhomogeneities of media.[6–10] These singularities are of fundamental interest because they reveal new aspects of light in complex fields. They also are a path to uncovering the vector fields in three dimensions, which contain knots and twists of the field vectors.[11,12] C-point singularities are fundamentally formed by the superposition of an optical vortex in one state of circular polarization, and a plane wave in the opposite state of polarization.[2,13] Thus, they provide a means for locating optical vortices, and for potentially using them in metrology, due to vortices' sensitivity to perturbations.[13,14] These beams are created by design, and can contain any polarization singularity that is desired. Preparation of designer beams with only one (isolated) singularity can be used to study its behavior with propagation.

Beyond the studies of polarization singularities, the technologies to study them lend to the development of a new type of remote sensing that adds polarization to imagery.[15] The natural world emits light with polarization information that is ignored by today's imaging systems. The advent of new ones with polarization imaging capabilities, in addition to space and wavelength, is expected to enhance the amount of information that is received.[16] Because polarization is multiplexed with wavelength, imaging polarimetry allows enhanced assessment in fields that range from geographical to medical.[17] A deep understanding of the polarization patterns[2,3,18] and the new family of hybrid modes that they entail[19] will be necessary to help in the interpretation of polarization-spatial-spectral imagery. Opening polarization to imaging will also help us uncover ways in which complex polarization patterns are present in nature,[20] and how the natural world uses polarization for its survival.[21]

As shown below, polarization-spatial modes are, in general, non-separable superpositions of polarization and spatial mode.[4] A study of classical polarization-spatial modes provides a way to recognize entangled states of individual photons.[22] Because spatial modes live in an infinite-dimensional Hilbert space, using spatial modes in the hyper-entanglement of photons increases the amount of information that can be encoded in a single photon. Here we present classical studies of the two-dimensional space of polarization "entangled" with a three-dimensional space of spatial-modes. Just the 3×2 dimensional state is hugely rich in patterns, which have parallels in the topology of Gaussian surfaces.[23,24]

In our previous work we aimed at making isolated singularities by preparing pure $p = 0$ LG beams.[18] We did this by modulating the amplitude of the diffractive pattern that created the spatial modes with an optical vortex. In this work we present singularities generated by unmodulated diffractive patterns, producing beams

Further author information: (Send correspondence to E.J.G.)
E.J.G.: E-mail: egalvez@colgate.edu, Telephone: 1 315 228 7205

in spatial modes that are not necessarily pure, but which still contain a well defined optical vortex. Section 2 presents the theoretical formalism for generating the beams with isolated singularities, and discuss further the properties of the space that we developed, which maps all 3×2 polarization singularities onto the surface of a sphere. Section 3 presents the experimental arrangement, and Sec. 4 presents the results.

2. THEORETICAL FRAMEWORK

We have previously shown that a superposition of Laguerre-Gauss (LG_p^ℓ) modes with topological charge ℓ of $+1$, -1 and 0 (and $p = 0$) can produce all types of isolated polarization singularities located in the center of the light's transverse plane.[18] They are constructed using a nonseparable superposition of polarization and spatial modes

$$\Psi = \left(\cos\beta\ LG_p^{+1} + \sin\beta\ LG_p^{-1} e^{\mathrm{i}\gamma}\right) e^{\mathrm{i}\delta}\ \hat{e}_R + LG_0^0\ \hat{e}_L, \tag{1}$$

where $\hat{e}_R$ and $\hat{e}_L$ denote states of right and left circular polarization, respectively. In this work we use r and ϕ as the transverse coordinates. The LG modes are given by

$$LG_p^\ell = A_{\ell,p} r^{|\ell|} \mathrm{e}^{\mathrm{i}\ell\phi} L_p^{|\ell|} GW. \tag{2}$$

The optical vortex of topological charge ℓ, located at the origin of the beam's transverse plane, is specified by the factor $r^{|\ell|}\exp(\mathrm{i}\ell\phi)$. LG beams carry a Gaussian envelope, given by $G = \exp(-r^2/w^2)$, with w being the beam's half width. The amplitude has a radial modulation given by the associated Laguerre polynomial $L_p^{|\ell|}$. Other terms in Eq. 2 are the normalization constant

$$A_{\ell,p} = \left(\frac{p!2^{|\ell|+1}}{\pi(|\ell|+p)!)}\right)^{1/2} \frac{1}{w^{|\ell|+1}}; \tag{3}$$

and the phase term $W = \exp[\mathrm{i}r^2/(2R) - \varphi]$, where R is the radius of curvature of the wavefront and φ is the Gouy phase. We ignore the phase term as we will not examine propagation effects. In the situations presented here the spatial mode that is generated for $\ell = \pm 1$ is mostly $p = 0$ with small admixtures of modes with $p \neq 0$. The generated beam thus had the form

$$\Psi = A_0 GW \left[\frac{\sqrt{2}r}{w}\left(\sum_p c_p L_p^1\right)\left(\cos\beta\ \mathrm{e}^{\mathrm{i}\phi} + \sin\beta\ \mathrm{e}^{\mathrm{i}(-\phi+\gamma)}\right)\mathrm{e}^{\mathrm{i}\delta}\ \hat{e}_R + \hat{e}_L\right]. \tag{4}$$

The state of polarization $\hat{e}$, expressed in terms of the circular basis is particularly convenient for our purposes:

$$\hat{e} = \mathrm{e}^{\mathrm{i}\theta}\cos\chi\hat{e}_R + \mathrm{e}^{-\mathrm{i}\theta}\sin\chi\hat{e}_L. \tag{5}$$

This is because χ and θ independently specify the shape and orientation of the ellipse, respectively. The ellipticity of the state is related to the ratio of the amplitudes of the polarization components via $\epsilon = \frac{b}{a} = \tan(\pi/4 - \chi)$, where a and b are the semimajor and semiminor axes of the ellipse, respectively. The orientation of the ellipse, or the angle that the semimajor axis of the ellipse forms with the x-axis, is half the phase difference between the two components, θ.

Using the construction of Eq. 1 we can map all types of C-points onto a unit sphere, shown in Fig. 1. The polar angle of the sphere is 2β and the azimuthal angle is γ. The patterns mapped by the sphere correspond to the case where $\delta = 0$. When $\delta \neq 0$, the pattern with (β, γ, δ) is the same as the pattern with $(\beta, \gamma - 2\delta, 0)$ but rotated by δ.

The sphere contains three regions of C-points. A lemon C-point consists of a state of circular polarization surrounded by elliptical states whose semi-major axis orientation (θ) increases with the angular coordinate. The north pole of the C-point sphere, obtained by setting $\beta = 0$ in Eq. 1, denotes the symmetric lemon, where $\theta = \phi/2 + \phi_0$, with ϕ_0 being an offset phase. The line patterns shown in the inserts to Fig. 1, also known as polarization lines, are the locus of semi-major axis directions. The top insert shows the polarization lines of the symmetric lemon. Lemons have one direction (ϕ_r) where all ellipses along it have $\theta = \phi_r$. That is, it is a

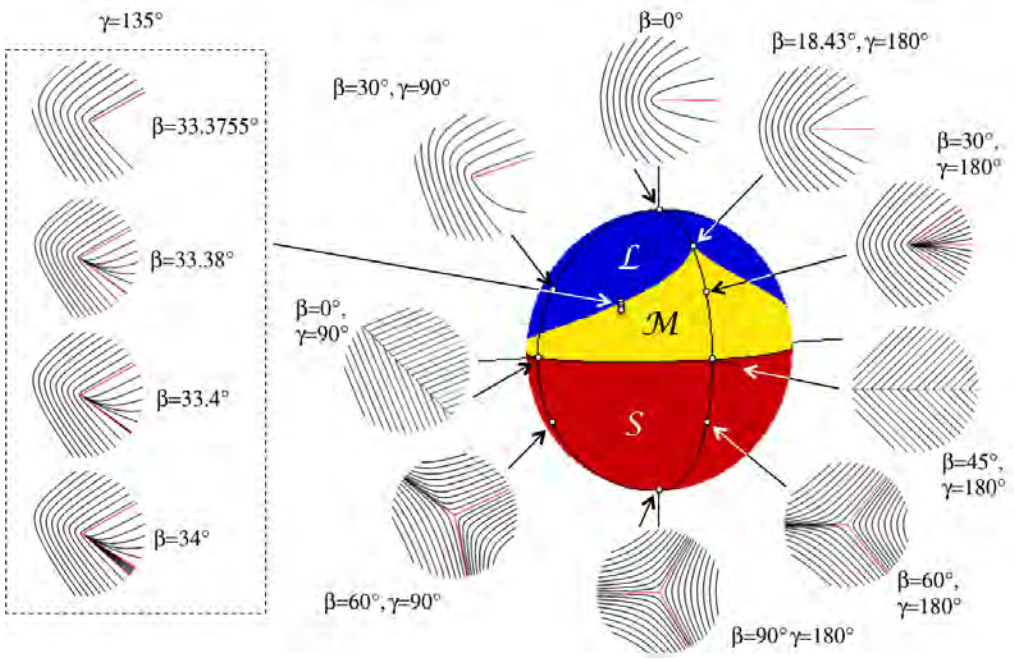

Figure 1. C-point sphere denoting by color the three morphological regions of C-points: lemons (L), monstars (M) and stars (S). The polar coordinates are 2β and γ (for $\delta = 0$), as specified by Eq. 1. Inserts show polarization lines corresponding to selected points on the sphere.

direction where the polarization line is radial. In the case of the symmetric lemon shown in the top insert of Fig. 1, $\phi_r = 0$ (for the case $\delta = 0$). More generally, the radial line of the symmetric lemon is $\phi_r = \delta/2$. (In the experiments we use this to set $\delta = 0$.) Lemons occupy a fraction of the northern hemisphere.

A second region of the C-point sphere covers the entire southern hemisphere, and represents all morphologies of C-point stars. In contrast to lemons, the polarization ellipses surrounding the C-point have an orientation that decreases with an increasing angular coordinate. They also have three radial polarization lines. The south pole ($\beta = \pi/2$) corresponds to the symmetric star. For this case the radial lines have an angular separation of $2\pi/3$. In general, the radial lines for symmetric stars are located at $\phi_{rn} = 2\pi n/3 - \gamma/2 + \delta/2$, where $n = 0, 1, 2$. The case of the insert to Fig. 1 corresponds to $\gamma = \pi$ and $\delta = 0$. When $\pi/4 < \beta < \pi/2$ the stars are asymmetric, with non-equidistant radial lines, as shown in the inserts to Fig. 1 with $\beta = 60°$.

In the northern hemisphere there is a region of intermediate type of C-points: monstars. The orientation of the ellipses surrounding monstars increases with the angular coordinate, similar to lemons; but similar to stars, monstars have three radial lines. The boundary between lemons and stars depends on γ, as seen in Fig. 1. Because θ is half of the phase difference between the two polarization components, then by setting $\theta = \phi$ in Eq. 4 we obtain a cubic equation in $\tan\phi$. The lemon-monstar boundary corresponds to solutions that yield three real roots where two are degenerate. The case for $\gamma = 135°$ is illustrated in the bounded insert: the top one is a lemon just before the boundary; the ones below it are a sequence of monstars, where we see the appearance of the degenerate roots and their splitting for points further away from the boundary. The case $\gamma = \pi$, where the monstar region has a cusp on the surface of the sphere, can be solved analytically, yielding $\beta_c = \tan^{-1}(1/3)$.[13]

Previous efforts map the C-points to a planar rectangle.[13,25] However, we find that a sphere is appropriate because the areas of the distinct types of C-points relate in a simple way to the density of C-points in random fields. Table 1 shows the computed areas of the three regions of the sphere of Fig. 1. The density of C-points in random fields is the area on the sphere weighted by the z-coordinate of the sphere (Υ in Ref. 25). Our numerical integration, listed in the table is in excellent agreement with predictions and measurements.[2,9]

An underlying structure of the C-point sphere is the sphere of first-order spatial modes,[26] where the north and south poles are the first-order Laguerre-Gauss modes, and the equator has first-order Hermite-Gauss modes

Table 1. Listing of normalized areas of the C-point regions and the density of C-points in random fields.

C-point	Area	Density
Lemon	0.382	0.447
Monstar	0.118	0.053
Star	0.5	0.5

of different orientations. In such a sphere, antipodes are orthogonal spatial modes. Similarly, any C-point morphology can be produced by a superposition of antipodal C-points. A recent implementation of C-points using Hermite-Gauss modes confirmed this.[18]

3. EXPERIMENTAL METHOD

The setup to produce isolated polarization singularities has been described before.[13] Briefly, a spatially filtered and expanded laser beam from a helium-neon laser (632.8 nm) was sent to a Mach-Zehnder type interferometer, as shown in Fig. 2a. The beam was linearly polarized in the vertical direction. A non-polarizing beam-splitter served as input port to the interferometer. Two parallel beams were formed by reflecting the beam that was reflected by the beam splitter.

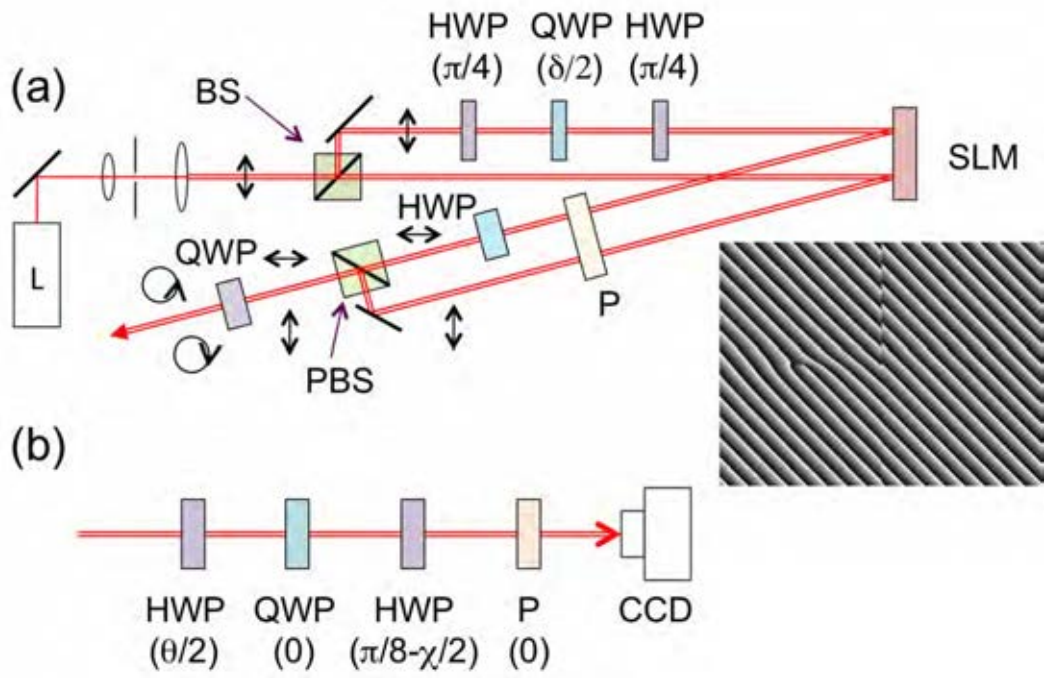

Figure 2. (a) Schematic of the apparatus used to prepare the beams, and (b) setup to measure the polarization patterns. Optical elements include beam splitters (non-polarizing BS; polarizing PBS), half-wave plate (HWP), quarter-wave plate (QWP), polarizer (P), digital camera (CCD) and spatial light modulator (SLM).

One of the beams passed through a 3-element Pancharatnam-Berry phase shifter, consisting of a rotating half-wave plate in between two quarter-wave plates with their axes aligned at 45° with respect to the horizontal. It introduced a geometric phase in the beam by three consecutive polarization-state transformations, which sent the state of polarization through a closed path on the Poincaré sphere. The phase shifter was used to adjust the phase δ in Eq. 1. A rotation of the half-wave plate by $\delta/2$ introduced a Pancharatnam-Berry phase of δ.[27]

Past the phase shifter, both beams were sent to a large area spatial light modulator (SLM, Holoeye model SR-2500). The SLM was programmed with two adjacent patterns, splitting it into two equal sized panes. Each

light beam hit the center of each pane. Both panes had phase diffraction gratings, shown in the insert to Fig. 2a, which diffracted the light by 0.5 degrees. The insert to the figure shows one type of patterns encoded onto the SLM, which were not amplitude modulated, as in a previous report.[18] The pattern in the left pane encodes a spatial mode with an asymmetric optical vortex, given by

$$f(r)\left(\frac{\sqrt{3}}{2}e^{\mathrm{i}\phi}-\frac{1}{2}e^{-\mathrm{i}\phi}\right), \tag{6}$$

Because the patterns were not modulated, the spatial mode was not a superposition of pure $p = 0$ modes with $\beta = \pi/6$ and $\gamma = \pi$. Thus, $f(r)$ accounts for the radial dependence of the mode, which is multi-ringed. This is an outcome that is seen in the experiments. The asymmetry in the forked pattern, which is responsible for creating the asymmetric optical vortex, is also visible in the figure. For illustration purposes, the pattern shown has a lower density of lines than the actual patterns.

Because the SLM modified the polarization state, we had a polarizer after the SLM, transmitting vertically polarized components of both beams. The $\ell = 0$ beam passed through a half-wave plate, which changed its polarization to horizontal. Both beams were recombined by a polarizing beam splitter. The beam exiting the interferometer passed through a quarter-wave plate that converted the two linearly polarized states into circularly polarized states, and thus constituting a mode given by Eq. 4.

The beam is analyzed using imaging polarimetry, which consists of sending the beam through a set of optical elements that serve as a polarization-state filter. Past the filter, the beam is imaged by a digital camera, as shown in Fig. 2b. By taking images after six filter settings we can find the Stokes parameters of every imaged point, and so determine the corresponding state of polarization.

4. RESULTS

We have taken data in a number of configurations. Here we show the results obtained by varying β in Eq. 4, and keeping $\gamma = \pi$ (via programming the pattern on the SLM) and $\delta = 0$ (via adjustment with the Pancharatnam-Berry phase shifter). As mentioned previously, we show data obtained by programming the SLM with an unmodulated pattern, giving rise to multi-ringed spatial modes.

Figure 3 shows theory and experimental results for an assortment of values of β. Three rows of frames are shown for each case. The top frame per case shows the polarization lines. The second frame contains the modeled pattern for the $p = 0$ case with a square array of ellipses representing the polarization of the point where it is drawn. The measurements are shown in the third frame per case. For the second and third frames, the color (online) represents the orientation of the ellipses, and the saturation of the color encodes the intensity of the light. Superimposed on the graphs are the calculated polarization ellipses. For the data we have chosen to display ellipses of points chosen at random. This is to avoid being biased by the prearranged square array. Finally, also superimposed on the frames are lines representing the calculated orientations of radial polarization lines.

The expectation is that when going from $\beta = 0$ to $\beta = 45°$, the asymmetry of the pattern increases. The same is the case when going from $\beta = 90°$ to $\beta = 45°$. Indeed, in looking at the set of eight sets of frames we see that the first and last cases ($\beta = 0$ and $\beta = 90°$, respectively) contain all colors of the colormap, but as β approaches 45° from either direction, certain colors (e.g., bright red and light blue) get compressed due to the rapid rate of change of θ as a function of ϕ around $\theta = 0$ and $\theta = 90°$.

A key aspect of the patterns is their distinction by the type of C-point that they contain. Those frames with $\beta = 0, 10°$ are lemon patterns; those with $\beta = 25°, 40°$ are monstars, and those with $\beta = 50°, 70°, 90°$ are stars. The case $\beta = 45°$ is a transitional case that does not contain a C-point. For $\beta \neq 45°$ the data is in good agreement with the general expectations. For example, the monstar and star cases in general agree with the expected patterns. The drawn radial lines also seem to agree with the patterns. Their orientations are listed in Table 2.

For the case $\beta = 45°$ the polarization orientations disagree with the drawn lines. In this case the lack of purity in the modes may play an important role.

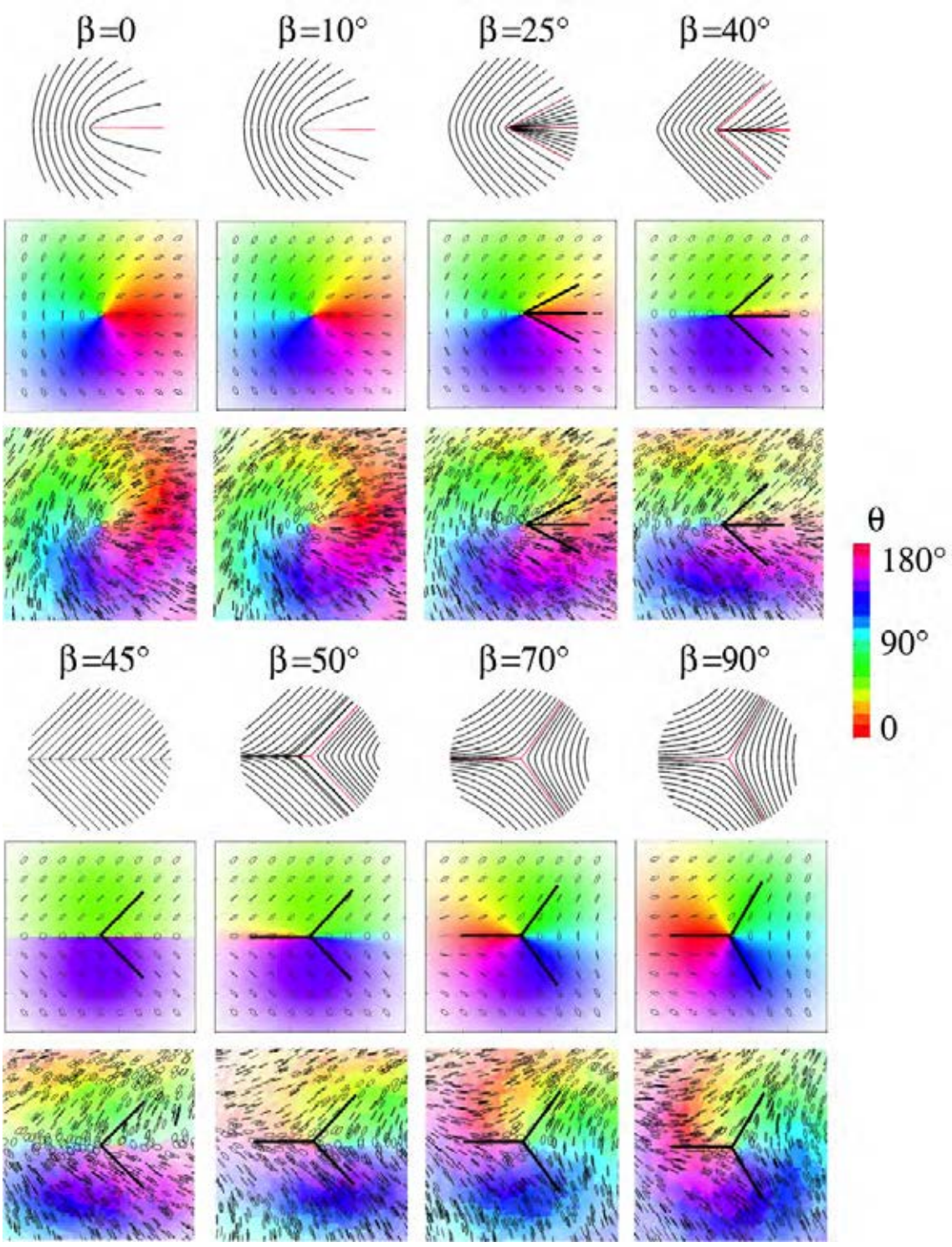

Figure 3. Theoretical and experimental results for selected values of β, with $\gamma = \pi$ and $\delta = 0$. For each case the top frame shows the calculated polarization lines; the middle frame shows the modeled pattern; and the bottom frame shows the experimental results. False color denotes the orientation of the polarization ellipses, and saturation represents intensity. Drawn ellipses represent the state of polarization; lines indicate the directions of radial polarization orientation.

The measured ellipticity of the experimental patterns also agrees with the modeled ones. Although the data has the usual imperfections of optical beams superimposed in an interferometer, the measured states of polarization are consistent with nearly (right) circular states close to the center of the pattern, the C-point, where the state is perfectly circular. As the distance from the C-point increases, the ellipticity increases, reaching linear states at about half way distance between the center and the edge of the frame. Past the linear-state region the handedness of the ellipses reverses to left-hand. The data and modelings also agree, although this may be taken as only approximately due to the lack of purity of the modes.

Table 2. Angles of the radial polarization orientation for the cases of Fig. 3. The case $\beta = 45$ has no C-point, but the two orientations of the polarization lines are shown for comparison with other cases. Angles are in degrees.

β	ϕ_{r1}	ϕ_{r2}	ϕ_{r3}
0	0		
10	0		
25	0	+27.5	−27.5
40	0	+42.2	−42.2
45		+45	−45
50	180	+47.3	−47.3
70	180	+54.3	−54.3
90	180	+60	−60

In the present work, we produce isolated C-points. It is possible to produce any desired number or type of C-points by design.[28] The use of other polarization bases, instead of the circular basis in Eq. 1, results in two C-points.[4] The use of higher-order Laguerre-Gauss modes instead of first-order modes, leads in principle to higher-order C-points.[3] In practice, we have found that the sensitivity of optical vortices to perturbations breaks up the C-points.

Moving forward, we have been experimenting with a same-path interferometer for producing better-quality patterns. The ones shown in this article suffer from the alignment problems, due to being a superposition of beams prepared in an interferometer. A same-path interferometer eliminates them.

An important use of beams with isolated C-points is in the study of the propagation of C-points through inhomogeneous or nonlinear media. Since C-points are produced by an underlying optical vortex in a circularly polarized field, they could be used to for the study of dynamics of optical vortices in media.

5. ACKNOWLEDGMENTS

We thank M.V. Berry, M.R. Dennis, V. Kumar, and N.K. Viswanathan for help and stimulating discussions. This work received funding from National Science Foundation grant PHY-0903972, and U.S. Air Force contract FA8750-11-2-0034.

REFERENCES

1. M.V. Berry, "Geometry of phase and polarization singularities, illustrated by edge diffraction and the tides," Proc. SPIE **4403**, 1-12 (2001).
2. M.R. Dennis, "Polarization singularities in paraxial vector fields: morphology and statistics," Opt. Commun. **213**, 201–221 (2002).
3. I. Freund "Polarization singularity indices in Gaussian laser beams," Opt. Commun. **201**, 251–270 (2002).
4. E.J. Galvez, S. Khadka, W.H. Schubert, and S. Nomoto, "Poincaré-beam patterns produced by nonseparable superpositions of LaguerreGauss and polarization modes of light," Appl. Opt. **51**, 2925–2934 (2012).
5. F. Cardano, E. Karimi, L. Marrucci, C. de Lisio, and E. Santamato, "Generation and dynamics of optical beams with polarization singularities," Opt. Express **21**, 8815–8820 (2013).
6. M.S. Soskin, V. Denisenko, and I. Freund, "Optical polarization singularities and elliptic stationary points," Opt. Lett. **28**, 1473–1477 (2003).

7. F. Flossmann, U.T. Schwarz, M. Maier, and M.R. Dennis, "Polarization Singularities from Unfolding an Optical Vortex through a Birefringent Crystal," Phys. Rev. Lett. **95**, 253901 1-4 (2005).
8. R.I. Egorov, M.S. Soskin, D.A. Kessler, and I. Freund, "Experimental Measurements of Topological Singularity Screening in Random Paraxial Scalar and Vector Optical Fields," Phys. Rev. Lett. **100**, 103901 1–4 (2008).
9. F. Flossmann, K. O'Holleran, M.R. Dennis, and M.J. Padgett, "Polarization Singularities in 2D and 3D Speckle Fields," Phys. Rev. Lett. **100**, 203902 1–4 (2008).
10. A.M. Beckley, T.G. Brown, and M.A. Alonso, "Full Poincaré beams," Opt. Express **18**, 10777–10785 (2010).
11. I. Freund, "Cones, spirals and Möbius strips, in elliptically polarized light," Opt. Commun. **249**, 7-22 (2005).
12. M.R. Dennis, "Fermionic out-of-plane structure of polarization singularities," Opt. Lett. **36**, 3765–3767 (2011).
13. E.J. Galvez, B.L. Rojec, and K.R. McCullough, "Imaging optical singularities: Understanding the duality of C-points and optical vortices," Proc. SPIE **8637**, 863706 1-10 (2013).
14. F. Ricci, W. Loffler, and M.P. van Exter, "Instability of higher-order optical vortices analyzed with a multi-pinhole interferometer," Opt. Express **20**, 22961–22975 (2012).
15. J.S. Tyo, D.L. Goldstein, D.B. Chenault, and J.A. Shaw, "Review of passive imaging polarimetry for remote sensing applications," Appl. Opt. **45**, 5453–5469 (2006).
16. D.A. Miller and E.L. Dereniak, "Selective polarization imager for contrast enhancements in remote scattering media," Appl. Opt. **51**, 4092–4102 (2012).
17. A. Pierangelo, A. Benali, A.-R. Antonelli, T. Novikova, P. Validire, B. Gayet, and A. De Martino, "*Ex-vivo* characterization of human colon cancer by Mueller polarimetric imaging," Opt. Express, **19**, 1582-1593 (2011).
18. E.J. Galvez, B.L. Rojec, V. Kumar, and N.K. Viswanathan, "Generation of isolated asymmetric umbilics in light's polarization," (to appear in Phys. Rev. A, 2014); arXiv:1402.5442.
19. G. Millione, H.I. Sztul, D.A. Nolan, and R.R. Alfano, "Higher-order Poincaré sphere, stokes Parameters, and the angular momentum of light," Phys. Rev. Lett. **107**, 053601 1-4 (2011).
20. M.V. Berry, M.R. Dennis, and R.L. Lee Jr., "Polarization singularities in the clear sky," New J. Phys 6, 162 1-14 (2004).
21. P.C. Brady, K.A. Travis, T. Maginnis, and M.E. Cummings, "Polarocryptic mirror of the lookdown as a biological model for open ocean camouflage," Proc. Natl. Acad. Sci. USA **110**, 9764-9769 (2013).
22. E.J. Galvez, "Proposal to produce two and four qubits with spatial modes of two photons," Proc. SPIE **8274**, 827415 1-5 (2012).
23. M.V. Berry and J.H. Hannay, "Umbilic points on Gaussian random surfaces," J. Phys. A **10**, 1809–1821 (1977).
24. T.H. Beuman, A.M. Turner, and V. Vitelli "Stochastic geometry and topology of non-Gaussian fields," Proc. Natl. Acad. Sci. USA **109**, 19943–19948 (2012).
25. M.R. Dennis, "Polarization singularity anisotropy: determining monstardom," Opt. Lett. **33**, 2572–2574 (2008).
26. M.J. Padgett and J. Courtial, "Poincaré-sphere equivalent for light beams containing orbital angular momentum," Opt. Lett. **24**, 430–432 (1999).
27. E.J. Galvez, "Applications of Geometric Phase in Optics" in *Recent Research Developments in Optics*, **2**, 165–182 (2002).
28. V. Kumar, G.M. Philip and N.K. Viswanathan, "Formation and morphological transformation singularities: Hunting the monstar," J. Opt. **15**, 044027,1–7 (2013).